Volume 201 May 2013 ISSN 0022-4596

ELSEVIER

JOURNAL OF SOLID STATE CHEMISTRY

IN THIS ISSUE:

Valence changes of manganese and structural phase transitions in $Sr_{1-x}Pr_xMnO_3$ ($0.1 \leq x \leq 0.6$)

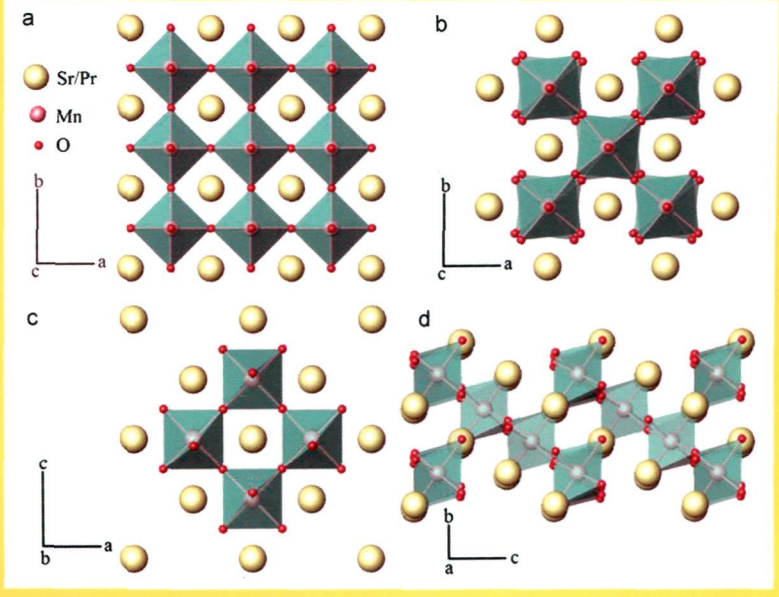

Teck-Yee Tan, Nicolas Martin, Qingdi Zhou, Brendan J. Kennedy, Qinfen Gu, Justin A. Kimpton, Zhaoming Zhang and Ling-Yun Jang

Journal of Solid State Chemistry

Volume 201, Pages 1-338 (May 2013)

editorial board/cover legend

Page IFC

Table of Contents - Web Colour Only

Pages iii-xi

Regular Articles

New pyridine-2,3,5,6-tetracarboxylato (H_4pdtc) complexes: Synthesis, crystal structures and magnetic properties of $K_2[Mn(H_2O)(pdtc)]\cdot 3H_2O$ 1, $Na_2[M_3(H_2O)_6(pdtc)_2]\cdot 6H_2O$ (M=Mn 2, Co 3)

Original Research Article

Pages 1-8

Yue-Qing Zheng, Hong-Lin Zhu, Jian-Li Lin, Wei Xu, Fang-Hong Hu

Graphic abstract

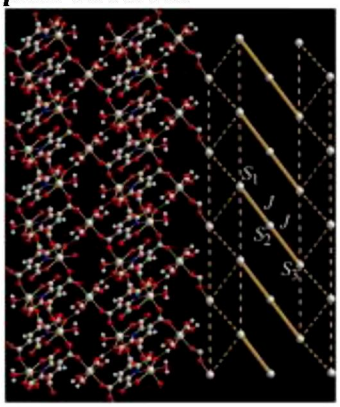

Highlights

► The characteristic building blocks of **1**–**3** are the pdtc bridged stair-like chains. ► The compound **2** and **3** are interlinked by trans-[***M***$(H_2O)_4]^{2+}$ moieties to 2D layers. ► The magnetic behavior of **1** was analyzed with zero-field splitting effects. ► The magnetic behaviors were modulated with linear trinuclear model for **2** and **3**.

A novel composite material based on antimony(III) oxide and amorphous silica

Original Research Article

Pages 9-12
Ludmila A. Zemnukhova, Alexander E. Panasenko

Graphical abstract

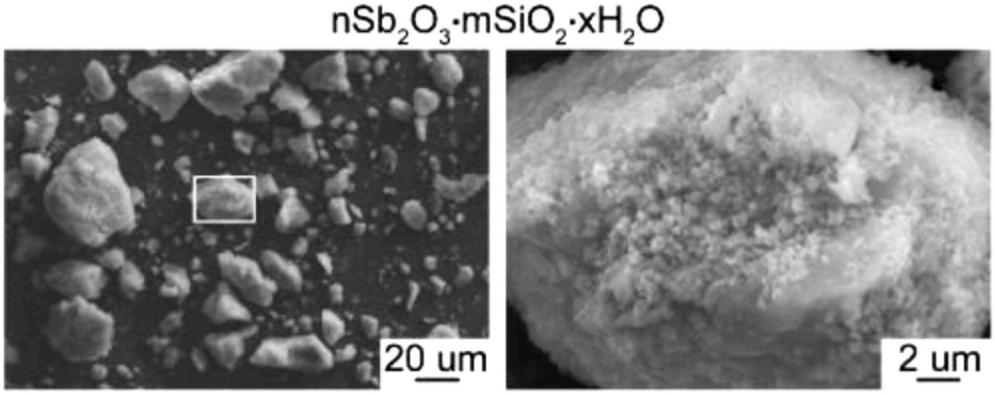

Highlights

► The composite material $n Sb_2O_3 \cdot m SiO_2 \cdot x H_2O$ was prepared in an aqueous medium. ► The composition of the material is controllable by a synthesis conditions. ► The morphology of the material and its optic properties have been determined.

Preparation and characterization of SiO_2:Sm^{3+} nanotube arrays with 1.06 μm laser antireflective property

Original Research Article

Pages 13-17
Wei-min Tan, Ning Huang, Li-jun Wang, Tian-shun Song, Chun-hua Lu, Liu-fang Wang, Jun-zhi Zhang

Graphical abstract

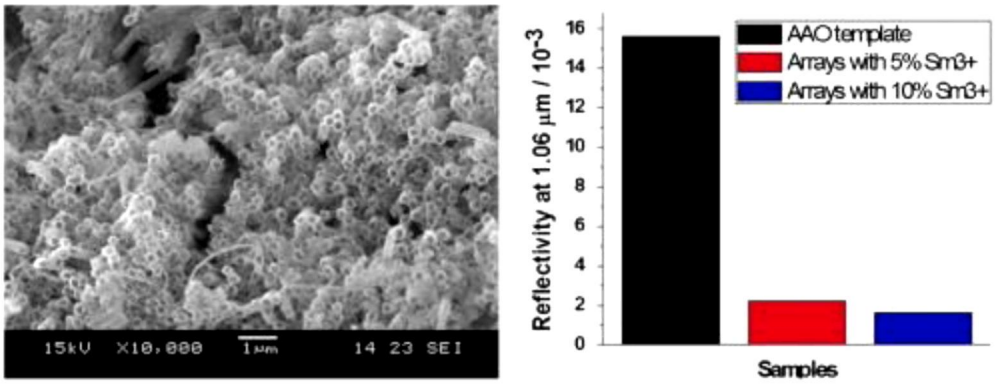

Highlights

► SiO_2:Sm^{3+} nanotube arrays are synthesized by a template-assisted sol–gel process. ► SiO_2:Sm^{3+} nanotube arrays have remarkable antireflective properties at 1.06 μm. ► The subwavelength structure results in a decrease of effective refraction index. ► The absorption performance of Sm^{3+} at 1.06 μm consume the energies of incident light.

Host absorption sensitizing and energy transfer to Eu^{3+} by Gd^{3+} in $Ba_6Gd_{2-x}Na_2Eu_x(PO_4)_6F_2$

Original Research Article

Pages 18-23

Mubiao Xie, Hongbin Liang, Yan Huang, Zhenhua Gao, Ye Tao

Graphical abstract

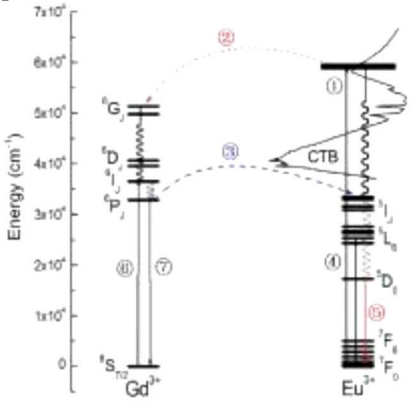

Highlights

► The Gd^{3+} ions play an important role in enhancing the host-related absorption in VUV range. ► The charge-transfer energy of Eu^{3+} decreases from Ca^{2+} to Sr^{2+} and Ba^{2+} in $M_6Gd_{1.90}Na_2Eu_{0.10}(PO_4)_6F_2$ (*M*=Ca, Sr, Ba). ► There is efficient energy transfer from Gd^{3+} to Eu^{3+} in $Ba_6Gd_{2-x}Na_2Eu_x(PO_4)_6F_2$.

Synthesis and structural characterization of a new chiral porous hybrid organic–inorganic material based on γ-zirconium phosphates and L-(+)-phosphoserine

Original Research Article

Pages 24-28

Hussein M.H. Alhendawi

Graphical abstract

• Red: oxygen

• White: zirconium

• Cyan: carbon

• Yellow: phosphorus

• Blue: nitrogen

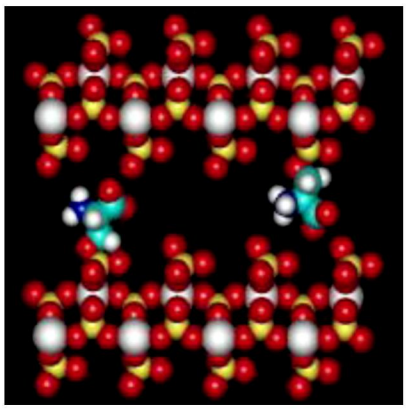

Highlights

► l-(+)-Phosphoserine (PS*) is exchanged with γ-ZrP by means of topotactic exchange. ► The maximum exchange level is 20%. ► γ-ZrP is functionalized with chiral amino acid group. ► γ-ZrP-PS* has large chiral space for huge guest molecules to be intercalated.

Boric acid flux synthesis, structure and magnetic property of $MB_{12}O_{14}(OH)_{10}$ *(M=Mn, Fe, Zn)*

Original Research Article

Pages 29-34

Dingfeng Yang, Rihong Cong, Wenliang Gao, Tao Yang

Graphical abstract

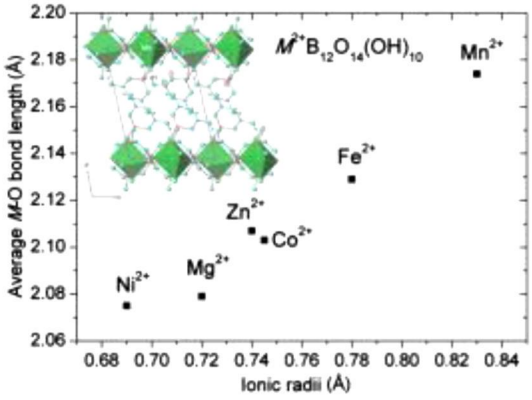

Highlights

► $MB_{12}O_{14}(OH)_{10}$ (*M*=Mn, Fe, Zn) are synthesized by two-step boric acid flux method. ► Single-crystal XRD was performed to determine the crystal structures in detail. ► Size of MO_6 (*M*=Mg, Mn, Fe, Co, Ni, Zn) agrees with the effective ionic radii. ► $MnB_{12}O_{14}(OH)_{10}$ is antiferromagnetic without a long-range ordering down to 2 K. ► DFT calculations indicate $ZnB_{12}O_{14}(OH)_{10}$ has a direct band gap 4.9 eV.

Characterization of carrier states in $CuWO_4$ *thin-films at elevated temperatures using conductometric analysis*

Original Research Article

Pages 35-40
Carlos M. Gonzalez, Jeffrey L. Dunford, Xiaomei Du, Michael L. Post

Graphical abstract

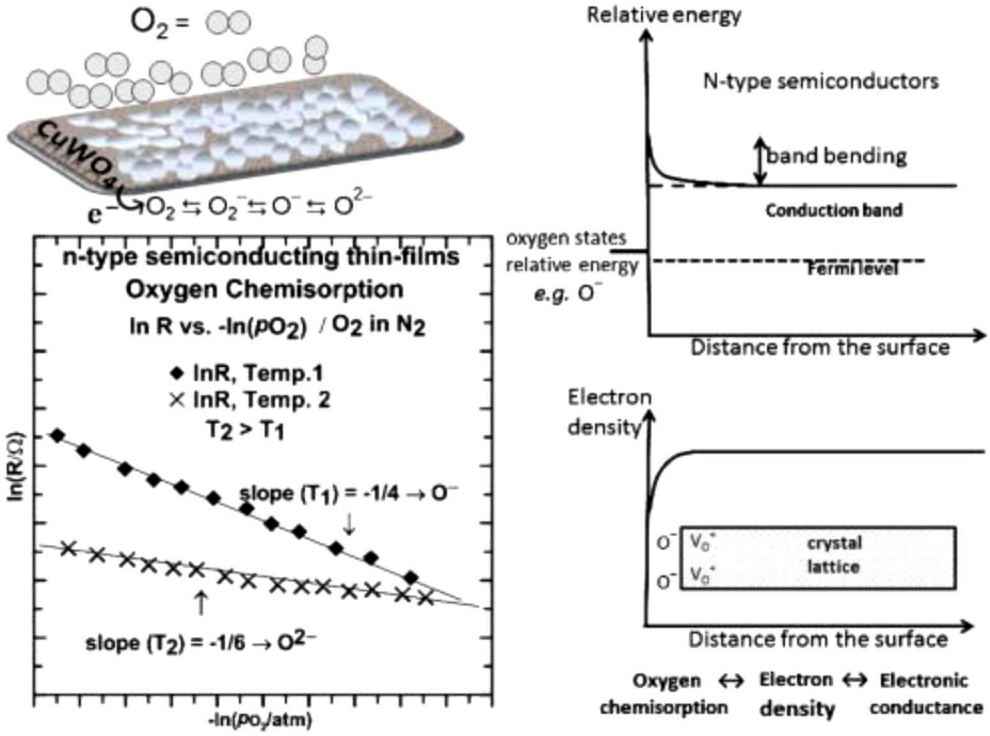

Highlights

► The study of surface species in $CuWO_4$ thin-films was carried using conductometry. ► The determination of the apparent activation energy of conduction with temperature is outlined. ► Temperature and O_2 concentration effects on the oxygen states was established. ► For the ranges of temperature studied, the identified operating oxygen states were O_2^- and O^-.

Incorporation effect of nanosized perovskite $LaFe_{0.7}Co_{0.3}O_3$ on the electrochemical activity of Pt nanoparticles-multi walled carbon nanotube composite toward methanol oxidation

Original Research Article

Pages 41-47
Meissam Noroozifar, Mozhgan Khorasani-Motlagh, Roghayeh Khaleghian-Moghadam, Mehri-Saddat Ekrami-Kakhki, Mohammad Shahraki

Graphical abstract

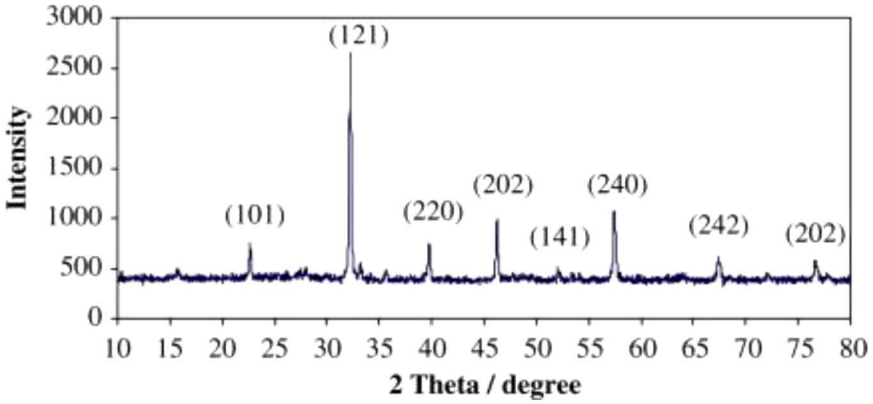

Highlights

► Nanocrystalline $LaFe_{0.7}Co_{0.3}O_3$ (LFCO) is prepared by a new simple co-precipitation method. ► Effect of LFCO to catalytic activity of PtNPS for methanol oxidation is studied. ► A synergistic effect is observed when LFCO is added to the Pt catalyst. ► Oxygen of LFCO could be considered as active oxygen to remove CO intermediates.

Effect of cation ordering on the electronic and lattice dynamic properties of Ag_2CdGeS_4 polytypes: First-principle calculation

Original Research Article

Pages 48-55

Lei Wei, Weiliu Fan, Yanlu Li, Xian Zhao, Lei Yang

Graphical abstract

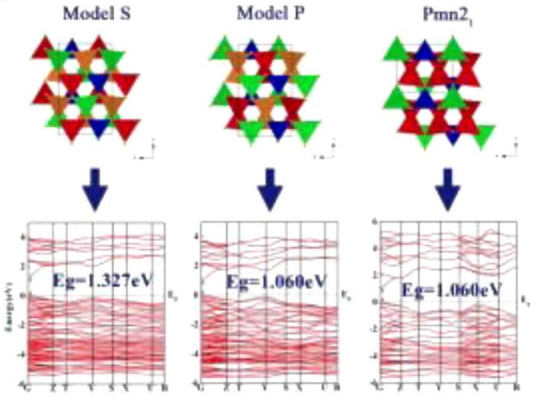

Highlights

► Structural configuration was focused other than compositional modulation. ► Establish the relationship between cation ordering and physicochemical properties. ► Explain the reason of different band gap with Born effective charges. ► Calculated infrared spectrum can be used to distinguish different polytypes.

Control of Y_2O_3 phase and its nanostructure formation through a very high energy mechanical milling

Original Research Article

Pages 56-62

M.K. Lee, E.K. Park, J.J. Park, C.K. Rhee

Graphical abstract

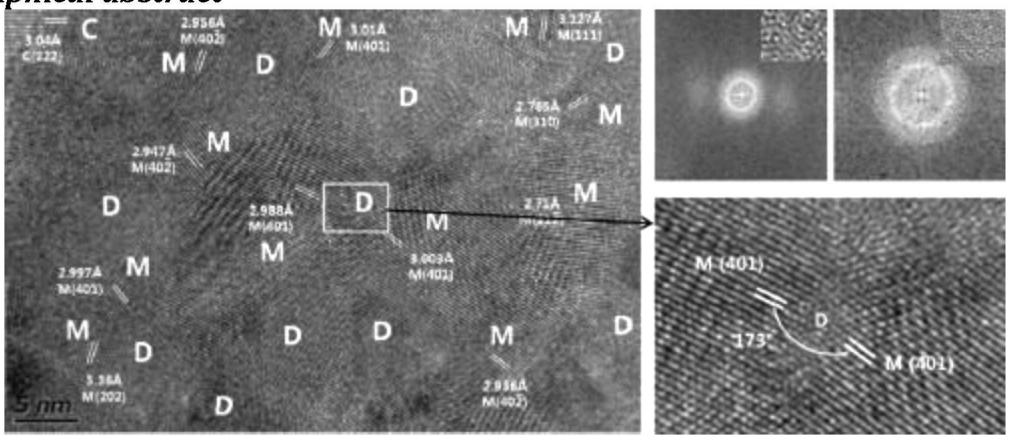

Highlights

► This paper analyses very high energy milling behavior of coarse Y_2O_3 particles. ► A drastic phase transition from cubic to monoclinic occurred with a partial amorphization. ► An existence of Y_2O_3 smaller than 10 nm is possible by forming strain-induced monoclinic crystals.

Unconventional critical magnetic behavior in the Griffiths ferromagnet $La_{0.4}Ca_{0.6}MnO_{2.8}\square_{0.2}$ oxide

Original Research Article

Pages 63-67

M. Triki, E. Dhahri, E.K. Hlil

Graphical abstract

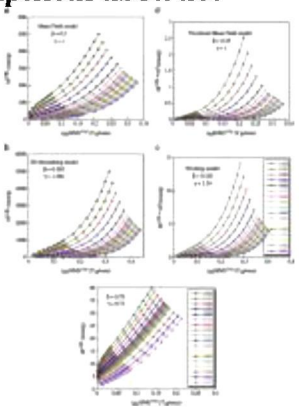

Highlights

► Study of the critical behavior for $La_{0.4}Ca_{0.6}MnO_{2.8}\square_{0.2}$ compound. ► A typical second-order magnetic transition near T_C. ► Unconventional critical exponents were found.

Thermodynamic studies of $CaLaFe_{11}O_{19}(s)$

Original Research Article

Pages 68-74

S.K. Rakshit, S.C. Parida, Kristina Lilova, Alexandra Navrotsky

graphical abstract

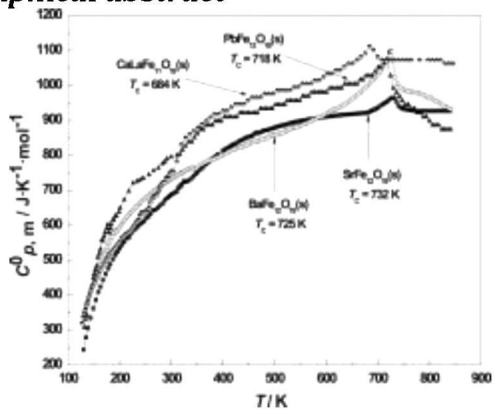

Highlights

► Thermodynamic studies on $CaLaFe_{11}O_{19}$(s) were performed using KEQMS and solution calorimetry. ► It was synthesized using gel combustion route and characterized by XRD technique. ► The compound is magnetic in nature and shows a heat capacity anomaly at 684 K. ► Thermodynamic table was constructed from 298 K to 1000 K.

Sb_2S_3 surface modification induced remarkable enhancement of TiO_2 core/shell nanowries solar cells

Original Research Article

Pages 75-78

Xiuqing Meng, Xiaozhou Wang, Mianzeng Zhong, Fengmin Wu, Yunzhang Fang

Graphical abstract

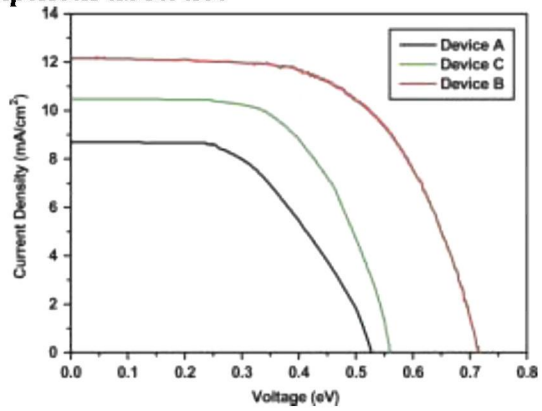

Highlights

► We fabricate sandwich structured TiO_2 dye-sensitized solar cells. ► The anode of the solar cells consist of Sb_2S_3 modified TiO_2 nanowire arrays/TiO_2 nanopartices. ► A solar conversion efficiency of 4.91% at 1 sun illumination is achieved. ► The high efficiency results from large surface area and expanded light adsorption of the anode.

Hydrothermal syntheses, crystal structures and characterization of new vanadoborates: The novel decorated cage cluster $[V_6B_{22}O_{44}(OH)_{10}]$

Original Research Article

Pages 79-84

Xing Liu, Jian Zhou, Litao An, Rong Chen, Feilong Hu, Qiuling Tang

Graphical abstract

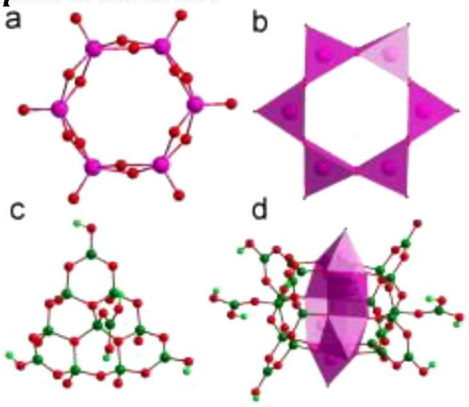

Highlights

► Novel decorated cage cluster $[V_6B_{22}O_{44}(OH)_{10}]$ is observed. ► The mixed valence vanadoborate cluster is found. ► The theoretical band structure and spectroscopic properties have been also studied.

Effects of ultrasound-related variables on sonochemically synthesized SAPO-34 nanoparticles

Original Research Article

Pages 85-92

Sima Askari, Rouein Halladj

Graphical abstract

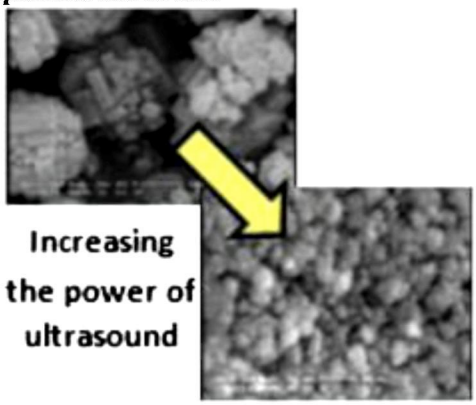

Highlights

► Effects of ultrasonic parameters on sonochemical synthesis of SAPO-34 nanoparticles. ► The higher crystallinity by increasing ultrasonic power, duration and sonication temperature. ► The

morphology changes from spherical aggregates of cubic particles to uniform nanospheres. ► Decreasing the particle size by increasing ultrasonic power, duration and sonication temperature.

Effect of synthesis atmosphere, wetting, and compaction on the purity of AlB_2

Original Research Article

Pages 93-100

Michael L. Whittaker, Raymond A. Cutler

Graphical abstract

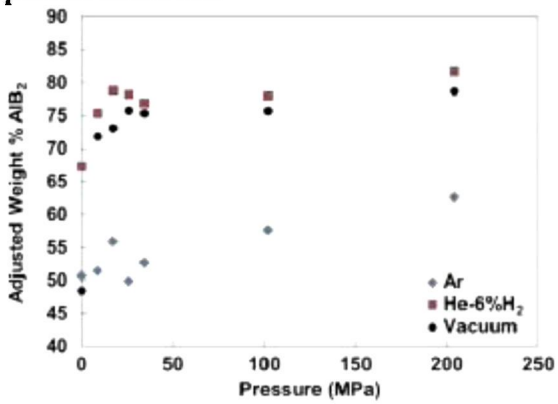

Highlights

► Vacuum or He–6% H_2 yielded higher AlB_2 than Ar due to reduced Al_2O_3. ► Compaction at 25 MPa prior to heating improved the AlB_2 yield. ► XRD can be used to quantify AlB_2 if Al is used to assess the free B content. ► Elimination of oxide impurities is the key to making higher purity AlB_2.

Investigation of Zr-doped BSCF perovskite membrane for oxygen separation in the intermediate temperature range

Original Research Article

Pages 101-106

Olga Ravkina, Tobias Klande, Armin Feldhoff

Graphical abstract

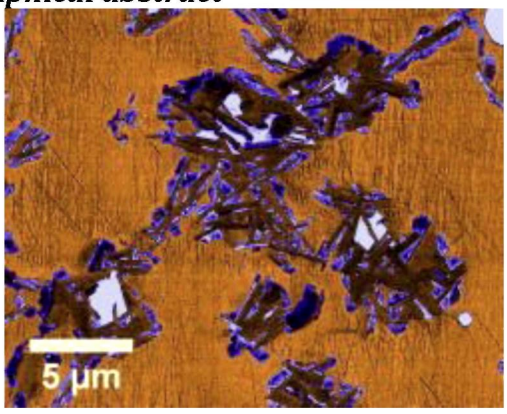

Highlights

► $Ba_{0.5}Sr_{0.5}Co_{0.8}Fe_{0.2}O_{3-\delta}$ systematically doped with increasing amount of zirconium. ► Cubic single-phase materials up to 3 wt% zirconium. ► Mixed $(Ba,Sr)ZrO_3$ by-phase formed mainly in the grain boundaries. ► Jänecke prism was proposed by XRD and EDXS data. ► $(Ba_{0.5}Sr_{0.5})(Co_{0.8}Fe_{0.2})_{0.97}Zr_{0.03}O_{3-\delta}$ showed a slight stabilization of oxygen flux as compared to pure $Ba_{0.5}Sr_{0.5}Co_{0.8}Fe_{0.2}O_{3-\delta}$.

Thermodynamic properties of $La_{1-x}A_xCoO_3$ (A=K, Cd, Pr and Nd)

Original Research Article

Pages 107-114

Rasna Thakur, N.K. Gaur

Graphical abstract

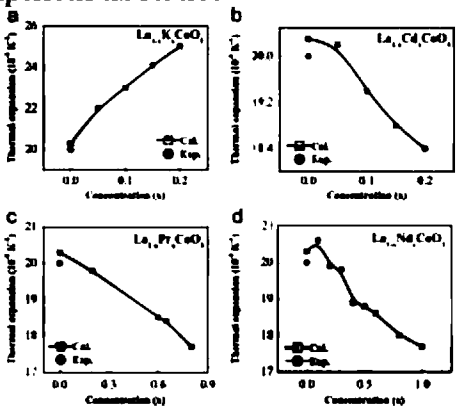

Highlights

► Probably the first report on the specific heat and thermal expansion in $La_{1-x}A_xCoO_3$. ► Thermal properties are computed using the MRIM probably for the first time. ► Effect of lattice distortions on bulk modulus and thermal properties is presented. ► The negative values of cohesive energy show the stability of these compounds.

Valence changes of manganese and structural phase transitions in $Sr_{1-x}Pr_xMnO_3$ ($0.1 \le x \le 0.6$)

Original Research Article

Pages 115-127

Teck-Yee Tan, Nicolas Martin, Qingdi Zhou, Brendan J. Kennedy, Qinfen Gu, Justin A. Kimpton, Zhaoming Zhang, Ling-Yun Jang

Graphical abstract

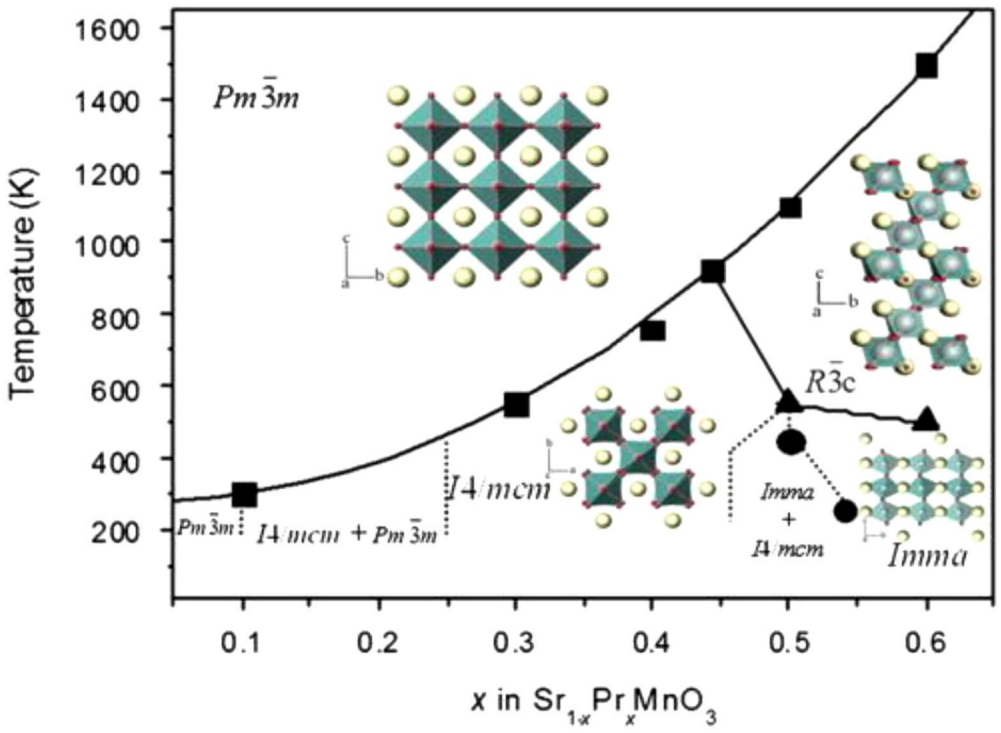

Highlights

► Structures of $Sr_{1-x}Pr_xMnO_3$, x=0.1–0.6, established using synchrotron XRD. ► Two first order phase transitions due to orbital ordering and the tilting of MnO_6 octahedra observed. ► High temperature phase transitions investigated. ► Valence state of Mn and Pr determined using XANES.

Redetermination of the structure of ALa_2WO_7 (A=Ba, Sr) with fluorite-like metal ordering

Original Research Article

Pages 128-132

W.T. Fu, D.J.W. IJdo, A. Bontenbal

Graphical abstract

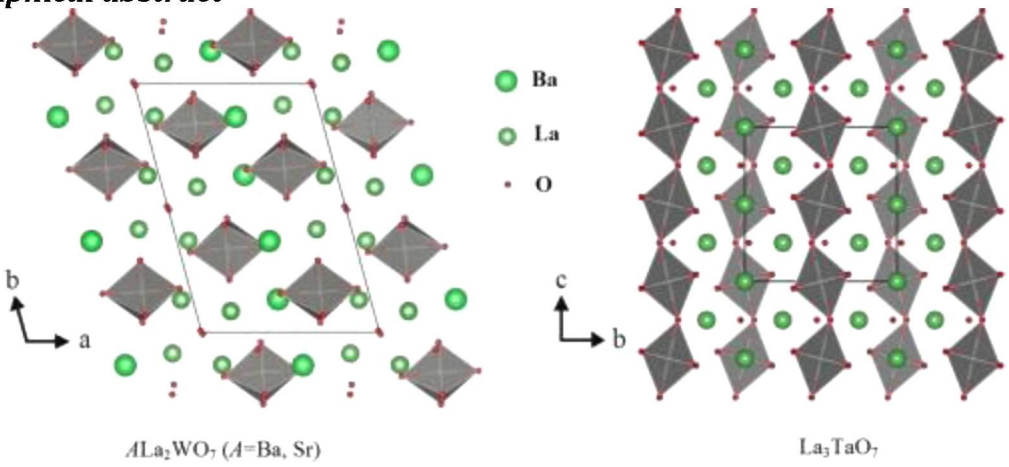

Highlights

► The structural ambiguity of $BaLa_2WO_7$ has been resolved. ► The details of the crystal structure of $SrLa_2WO_7$ are reported for the first time. ► ***A***La_2WO_7 (***A***=Ba, Sr) closely resemble β-La_3RuO_7 and one of the La_3IrO_7 polymorph.

Synthesis, crystal structure, and magnetic properties of bis(aqua)[μ-(terepthalato-κo,κo')]copper(II)monohydrate $[Cu(C_8O_4)(OH_2)_2]\cdot H_2O$

Original Research Article

Pages 133-136

Emmanuel N. Nfor, Felicite Majoumo-Mbe, Peter T. Ndifon, Emmanuel O. Duke, Evans N. Mainsah, Offiong E. Offiong, Ededet A. Eno

Graphical abstract

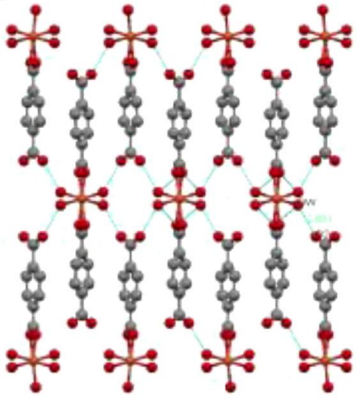

Highlights

► A novel copper(II) coordination polymer with terepthalate dianion was grown in an aqueous solution. ► The single crystal growth temperature was 25 °C for period of two weeks. ► The magnetic property of the complex was studied using SQUID. ► The complex showed antiferromagnetic properties.

Core–shell TiO_2 microsphere with enhanced photocatalytic activity and improved lithium storage

Original Research Article

Pages 137-143

Hong Guo, Dongxue Tian, Lixiang Liu, Yapeng Wang, Yuan Guo, Xiangjun Yang

Graphical abstract

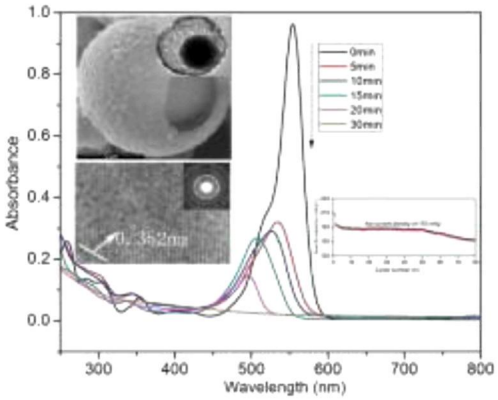

Highlights

► TiO_2 mesospheres are synthesized by solvothermal alcoholysis. ► It is core–void–shell structure and the thickness of shell is estimated to 80 nm. ► It exhibits a remarkable photocatalytic activity and improved lithium storage.

Iron oxide nanoparticles: the Influence of synthesis method and size on composition and magnetic properties

Original Research Article

Pages 144-152

M.D. Carvalho, F. Henriques, L.P. Ferreira, M. Godinho, M.M. Cruz

Graphical abstract

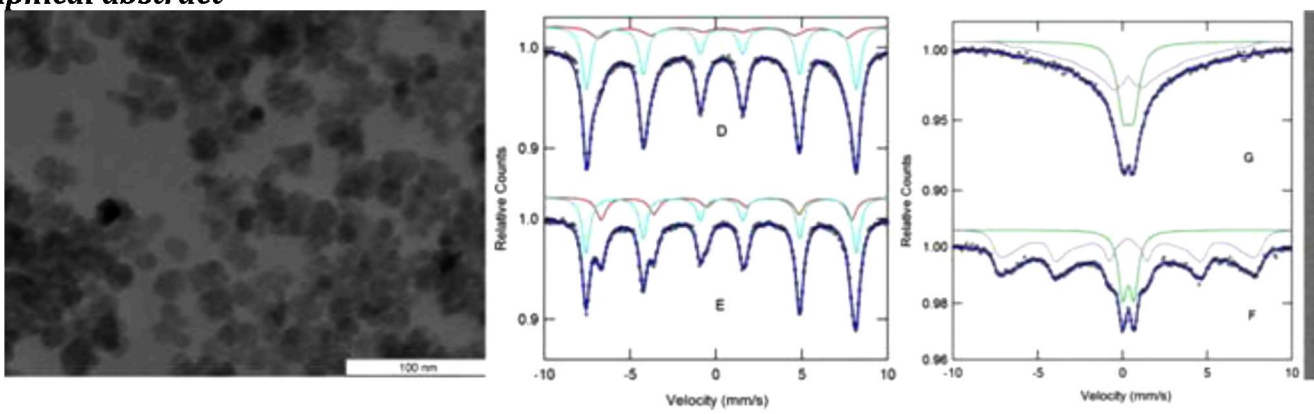

Highlights

► $Fe_{3-x}O_4$ nanoparticles with a mean size between 7 and 20 nm were synthesized. ► The smallest nanoparticles were obtained by a reduction precipitation method, under air. ► The increase of particles size was succeeded using a hydrothermal treatment at 150 °C. ► The magnetic properties of the nanoparticles are directly related with their size.

Synthesis of crumpled nanosheets of polymeric carbon nitride from melamine cyanurate

Original Research Article

Pages 153-163

Roberto C. Dante, Pablo Martín-Ramos, F.M. Sánchez-Arévalo, L. Huerta, M. Bizarro, Luis M.

Navas-Gracia, Jesús Martín-Gil

Graphical abstract

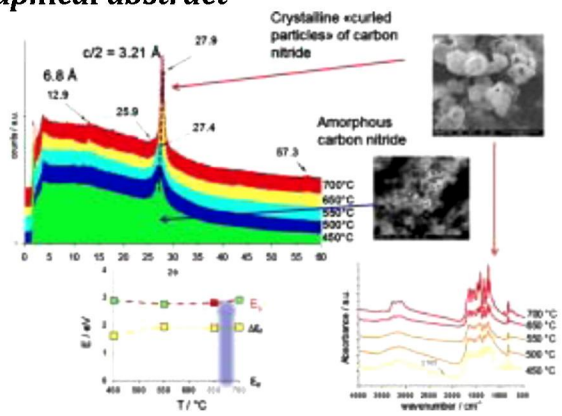

Highlights

► We synthetized carbon nitride using melamine cyanurate. ► The reaction of carbon nitride formation is catalyzed by sulfuric acid. ► The carbon nitride obtained at 700 °C is composed of globular particles. ► The material obtained at 700 °C is a ***n***-type semiconductor.

In situ X-ray and neutron diffraction of the Ruddlesden–Popper compounds $(RE_{2-x}Sr_x)_{0.98}(Fe_{0.8}Co_{0.2})_{1-y}Mg_yO_{4-\delta}$ *(RE=La, Pr): Structure and* CO_2 *stability*

Original Research Article

Pages 164-171

C. Chatzichristodoulou, B.C. Hauback, P.V. Hendriksen

Graphical abstract

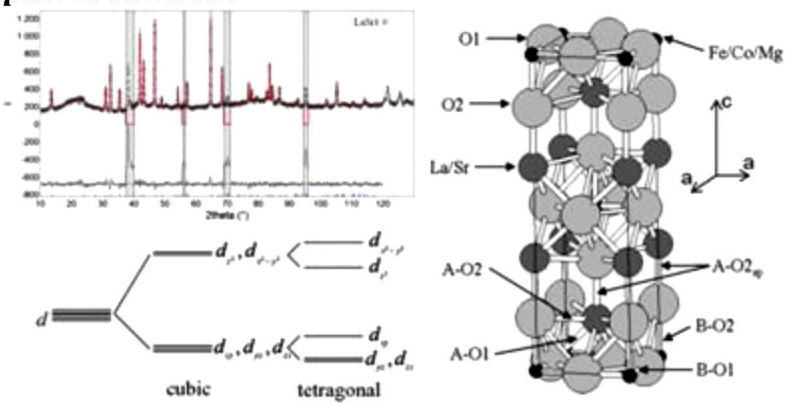

Highlights

► The thermal and chemical expansion coefficients are largely anisotropic. ► The expansion of the perovskite layers is constrained along the ***a*** direction. ► The studied compositions show remarkable thermodynamic stability upon reduction. ► The thermal and chemical expansion coefficients are lower than related perovskites. ► The investigated materials decompose in CO_2 containing atmospheres.

3D Rare earth porous coordination frameworks with formamide generated in situ syntheses: Crystal structure and down- and up-conversion luminescence

Original Research Article

Pages 172-177

Xue Ma, Jing Tian, Hong-Y. Yang, Kai Zhao, Xia L

Graphical Abstract

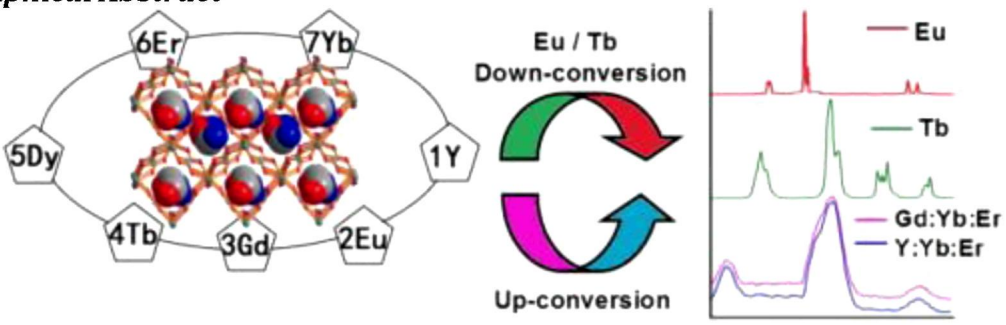

Highlights

► The reaction of $RE(NO)_3 \cdot 6H_2O$ and formamide produced complexes $[RE(HCOO)_4]^-[NH_2CHNH_2]^+$. ► The complexes possess 3D frameworks with the 1D channels occupied by $[NH_2CHNH_2]^+$ cations. ► Eu(III)/Tb(III) complexes display the characteristic down-conversion emission of Ln(III) ions. ► The Y:Yb,Er and Gd:Yb,Er doped complexes exhibit the up-conversion emission.

Solid solution studies of layered honeycomb-ordered phases O_3–$Na_3M_2SbO_6$ (M=Cu, Mg, Ni, Zn)

Original Research Article

Pages 178-185

Whitney Schmidt, Romain Berthelot, A.W. Sleight, M.A. Subramanian

Graphical abstract

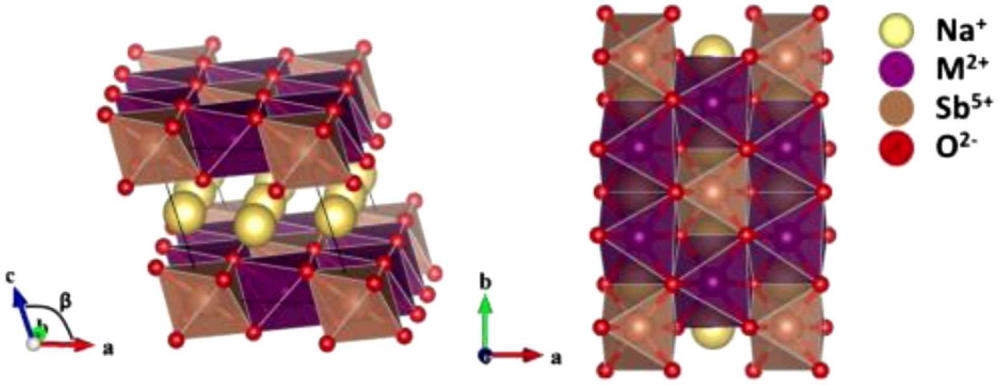

Highlights

► The solid solutions O_3–$Na_3M_{2-x}M'_xSbO_6$(*M*, *M'*=Cu, Mg, Ni, Zn) were synthesized. ► These compounds crystallize in the *C*2/*m* space group. ► The Jahn–Teller active Cu^{2+} causes distortion of the

monoclinic cell. ► The Cu^{2+} spin gap magnetic properties are diluted upon 25% substitution. ► All compositions are insulating and have large band gaps.

High-pressure crystal growth and electromagnetic properties of 5d double-perovskite Ca_3OsO_6

Original Research Article

Pages 186-190

Hai Luke Feng, Youguo Shi, Yanfeng Guo, Jun Li, Akira Sato, Ying Sun, Xia Wang, Shan Yu, Clastin I. Sathish, Kazunari Yamaura

Graphical Abstract

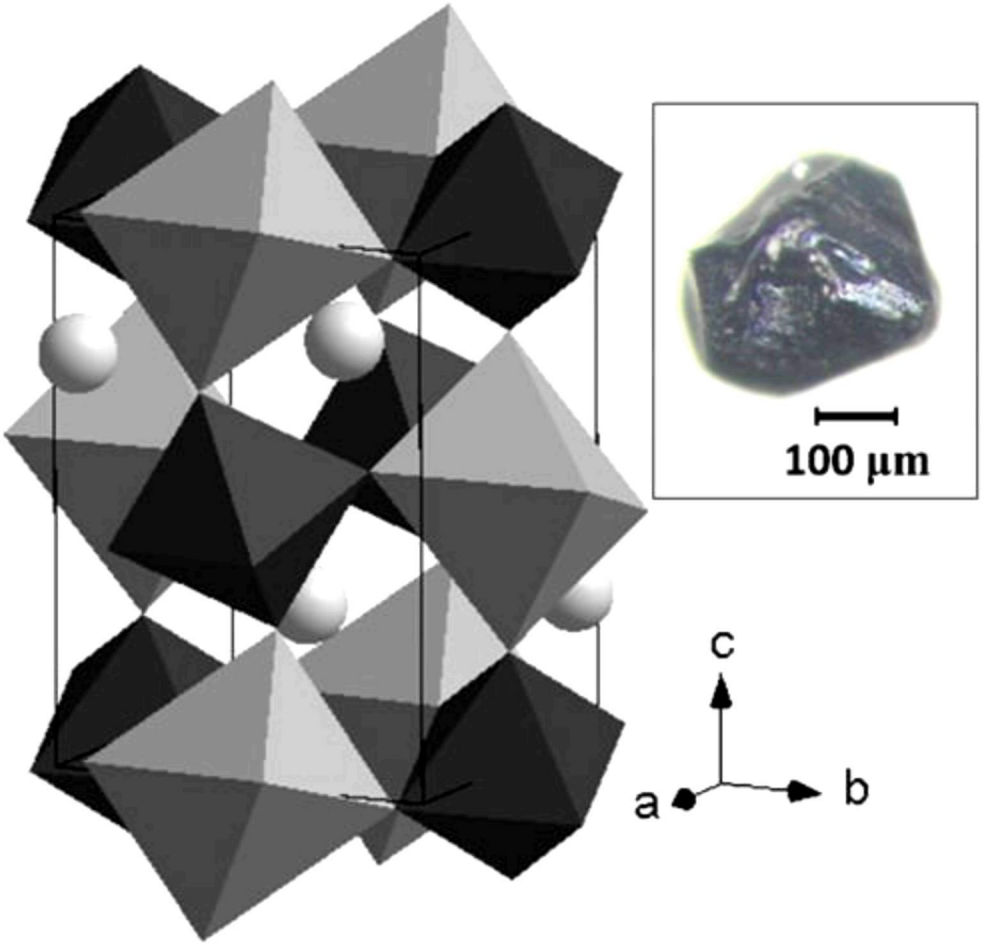

Highlights

► Single crystals of Ca_3OsO_6 have been successfully grown under high-pressure. ► Ca_3OsO_6 crystalizes into an ordered double-perovskite structure. ► The Ca_3OsO_6 undergoes an antiferromagnetic transition at 50 K.

Rare-earth metal gallium silicides via the gallium self-flux method. Synthesis, crystal structures, and magnetic properties of RE$(Ga_{1-x}Si_x)_2$ *(RE=Y, La–Nd, Sm, Gd–Yb, Lu)*

Original Research Article

Pages 191-203

Gregory M. Darone, Benjamin Hmiel, Jiliang Zhang, Shanta Saha, Kevin Kirshenbaum, Richard Greene, Johnpierre Paglione, Svilen Bobev

Graphical abstract

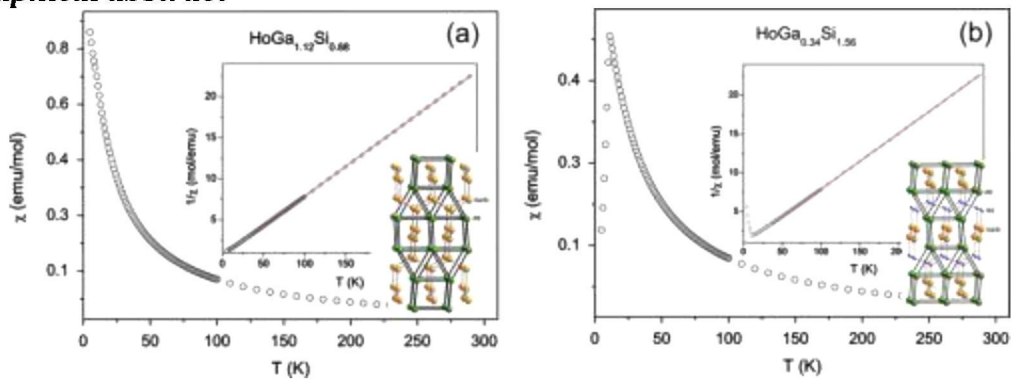

Highlights

► Light rare-earth gallium silicides crystallize in α-$ThSi_2$ structure type. ► Heavy rare-earth gallium silicides crystallize in α-$GdSi_2$ structure type. ► LuGaSi crystallizes in a defect variant of the $YbMn_{0.17}Si_{1.83}$ structure type.

Structure and electronic properties of a Mn nanowire encapsulated in carbon nanotubes

Original Research Article

Pages 204-207

C. Paduani

Graphical abstract

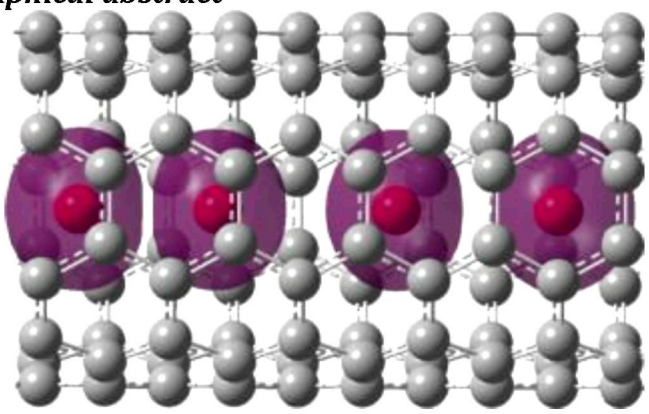

Highlights

► A Mn nanowire can be stabilized in a single-walled armchair carbon nanotube. ► The ground state is ferromagnetic. ► The average moment on the Mn atoms is $4.35\ \mu_B$. ► A polarized spin channel is identified for conduction electrons in the filled nanotube.

Preparations, structures and properties of heterobimetallic complexes based on tetrahydrofuran-2,3,4,5-tetracarboxylate

Original Research Article

Pages 208-214

Tian-Jing Jia, Shu-Mu Li, Wei Cao, Li-Cun Li, Xiang-Jun Zheng, Da-Qiang Yuan

Graphical abstract

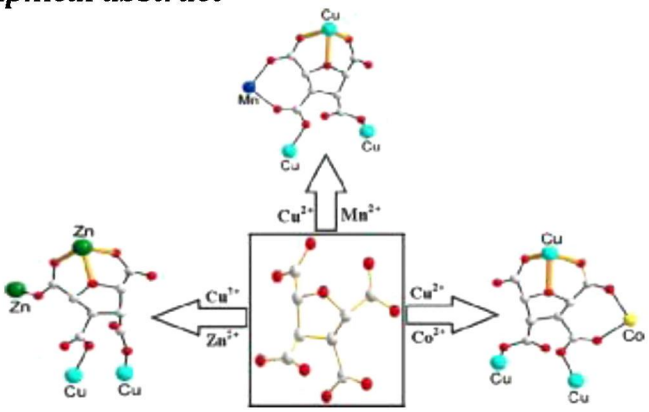

Highlights

► Complexes **1** and **3** contain 2-D wave-like negative-charged layers. ► Complex **2** is a 2-D neutral layer structure with a $\{8\}_2\{8^4;12^2\}$ topology. ► Complexes **1**–**3** are the first example of heterobimetallic MOFs based on FTA. ► The coordination sites of FTA show size-selectivity to metal ions.

Cadmium(II) and Copper(II) coordination polymers based on 5-(Pyrazinyl) tetrazolate ligand: Structure, photoluminescence, theoretical calculations and magnetism

Original Research Article

Pages 215-221

Hui-Fen Chen, Wen-Bin Yang, Lang Lin, Xiang-Guang Guo, Xue-jing Dui, Xiao-Yuan Wu, Can-Zhong Lu, Cui-Juan Zhang

Graphical abstract

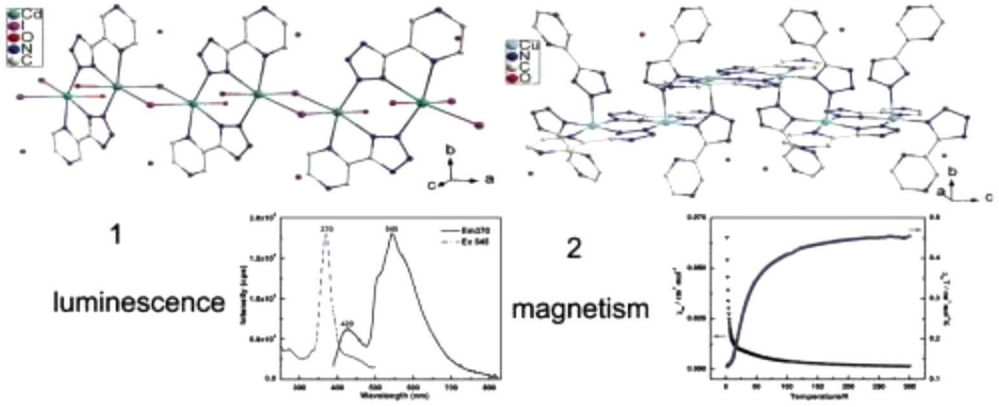

Highlights

► We report two novel 1D μ_2-tetrazolyl bridged Cd(II) and Cu(II) compounds. ► The cadmium(II) compound exhibits a green luminescence. ► Theoretical calculations were conducted to elucidate the green luminescence. ► The Cu(II) compound exhibits an anti-ferromagnetic ordering.

Structural and spectroscopic properties of high temperature prepared ZrO_2–TiO_2 mixed oxides

Original Research Article

Pages 222-228

Chiara Gionco, Alfio Battiato, Ettore Vittone, Maria Cristina Paganini, Elio Giamello

Graphical abstract

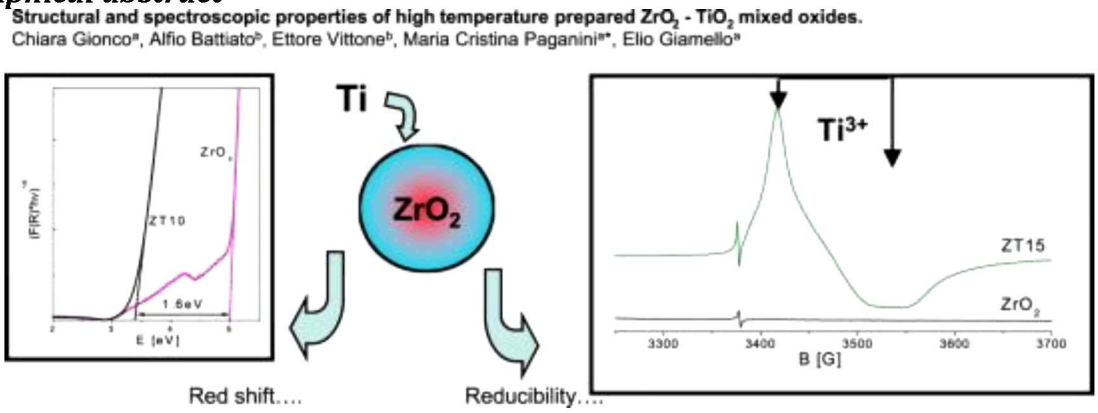

Highlights

► ZrO_2–TiO_2 mixed oxides have been prepared via sol–gel synthesis. ► Solids with low Ti loading are constituted by the monoclinic phase of ZrO_2. ► The presence of Ti ions modify the electronic structure of the solid. ► The introduction of titanium ions increases the reducibility of the solid.

The site-selective excitation and the dynamical electron–lattice interaction on the luminescence of YBO_3: Sb^{3+}

Original Research Article

Pages 229-236

Lei Chen, An-Qi Luo, Yao Zhang, Xin-Hui Chen, Hao Liu, Yang Jiang, Shi-Fu Chen, Kuo-Ju Chen, Hao-Chung Kuo, Ye Tao, Guo-Bin Zhang

Graphical abstract

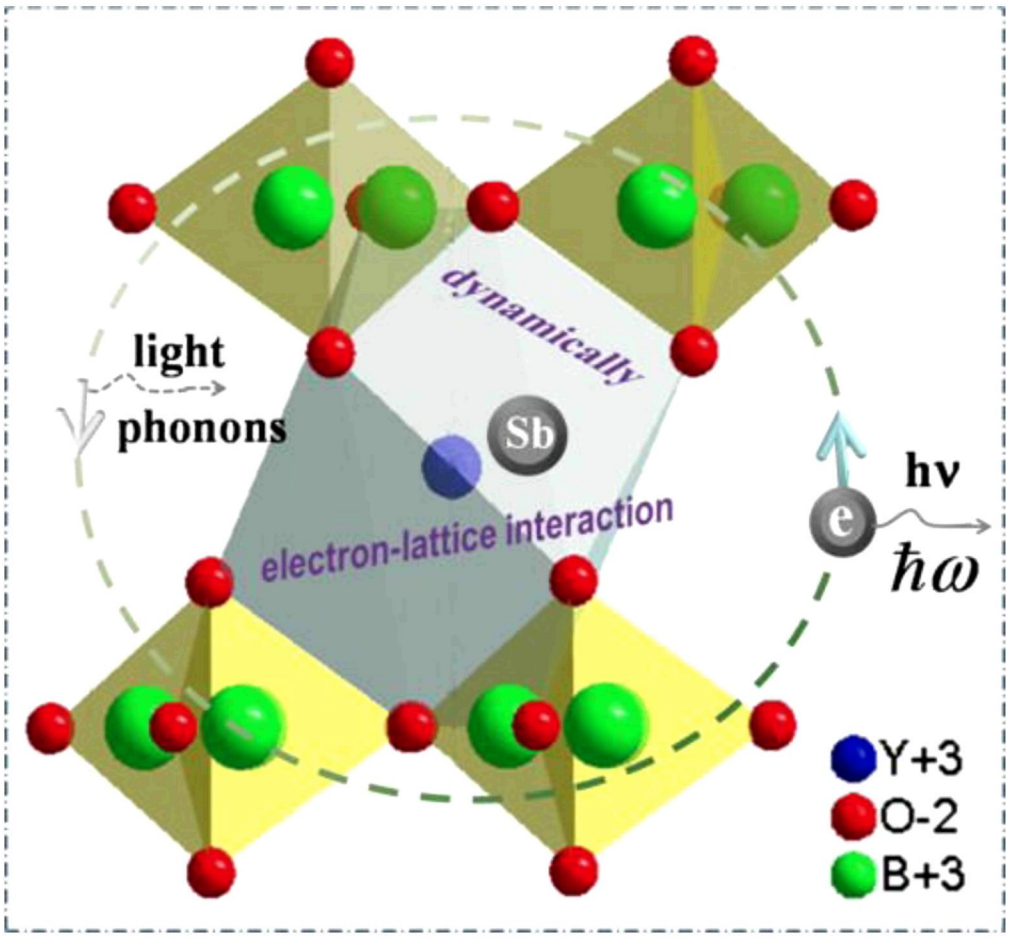

Highlights

► The site-selective excitation of YBO_3: Sb^{3+} was demonstrated. ► The temperature-dependent luminescence of YBO_3: Sb^{3+} was observed. ► Strong electron–lattice interaction between the Sb^{3+} and YBO_3 host was revealed. ► Superposition of the Jahn–Teller effect and site-selective excitation was discriminated. ► Optical parameters were calculated by using a molecular orbital approximation.

Vanadium oxide nanotubes VOx-NTs: Hydrothermal synthesis, characterization, electrical study and dielectric properties

Original Research Article

Pages 237-243

H. Nefzi, F. Sediri

Graphical abstract

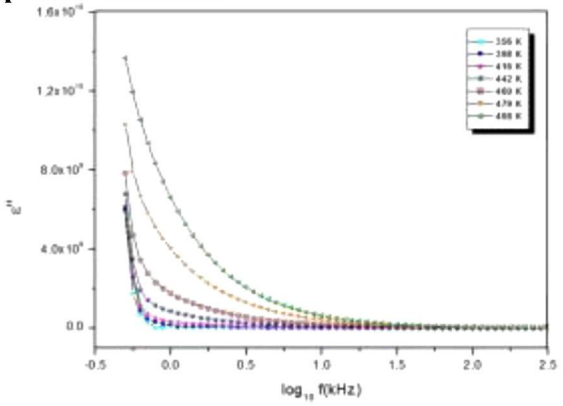

$Pd_2Cd_{11-\delta}$ (0.21≤δ≤0.51)–a partly disordered γ-brass type phase and $Pd_{0.238}Cd_{0.762}$-a γ-brass related incommensurate phase in the palladium–cadmium system

Original Research Article

Pages 244-249

Partha Pratim Jana, Sven Lidin

Graphical abstract

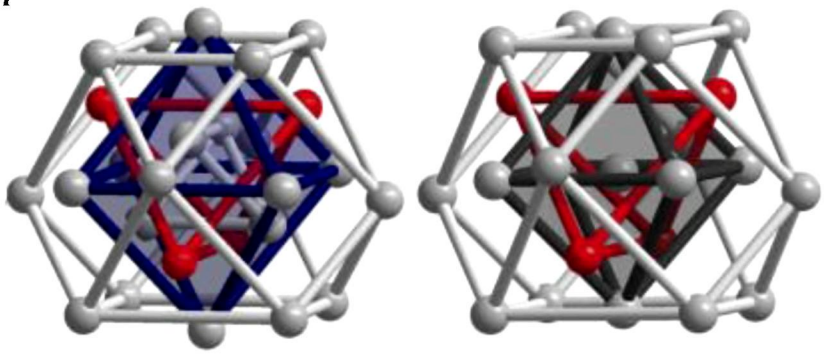

Highlights

► Partly disordered ***γ***-brass type $Pd_2Cd_{11-\delta}$ (0.21≤***δ***≤0.51) and ***γ***-brass related $Pd_{0.238}Cd_{0.762}$ have been synthesized. ► The $Pd_2Cd_{11-\delta}$ structure have been described by cluster concept. ► Incommensurately modulated $Pd_{0.238}Cd_{0.762}$ have been described by (3+1) D space description. ► The structure of $Pd_{0.238}Cd_{0.762}$ has two different chains of atomic subunits, each with their own translational periodicities.

Site preference, magnetism and lattice vibrations of intermetallics $Lu_2Fe_{17-x}T_x$ (T=Cr, Mn, Ru)

Original Research Article

Pages 250-255

Jin-Chun Li, Ping Qian, Zhen-Feng Zhang, Xiao-Jian Yuan, Yi-Wen Wang, Jiang Shen, Nan-Xian Chen

Graphical abstract

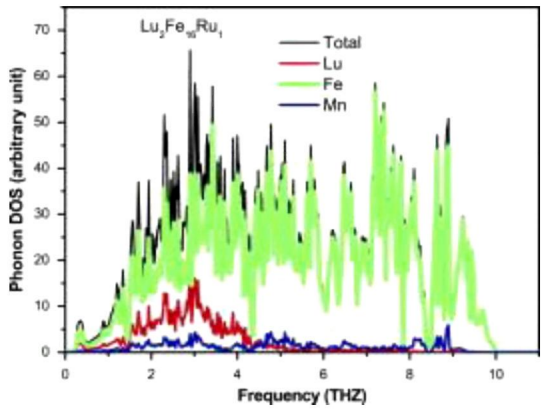

Highlights

► There are no reports on lattice vibrations of $Lu_2(Fe, \boldsymbol{T})_{17}$ (***T***=Cr, Mn, Ru) compounds. ► The phase stability and site preference are evaluated first for the complex structures of $Lu_2(Fe, \boldsymbol{T})_{17}$ (***T***=Cr, Mn, Ru) compounds. ► The lattice inversion method to obtain the interatomic pair potential is the unique one.

High temperature behavior of zirconium germanates

Original Research Article

Pages 256-261

A.V. Utkin, N.I. Baklanova, I.G. Vasilyeva

Graphical abstract

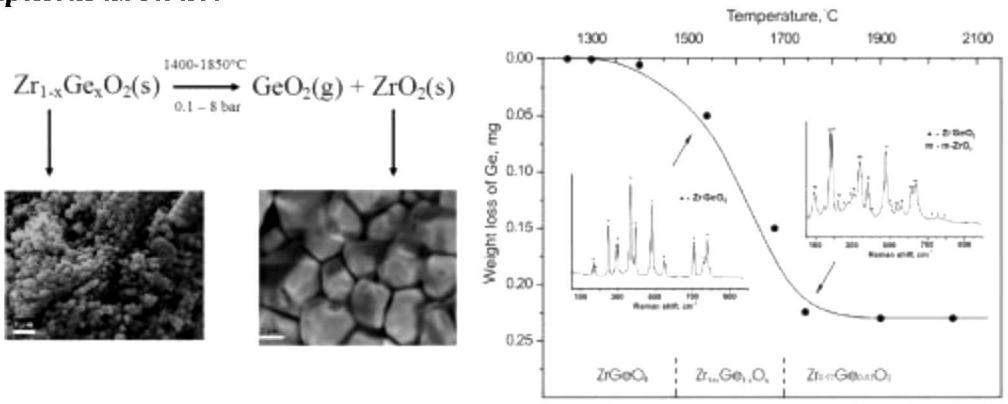

The effect of structural vacancies on the thermoelectric properties of $(Cu_2Te)_{1-x}(Ga_2Te_3)_x$

Original Research Article

Pages 262-269

Zuxin Ye, Jung Young Cho, Misle M. Tessema, James R. Salvador, Richard A. Waldo, Hsin Wang, Wei Cai

Graphical abstract

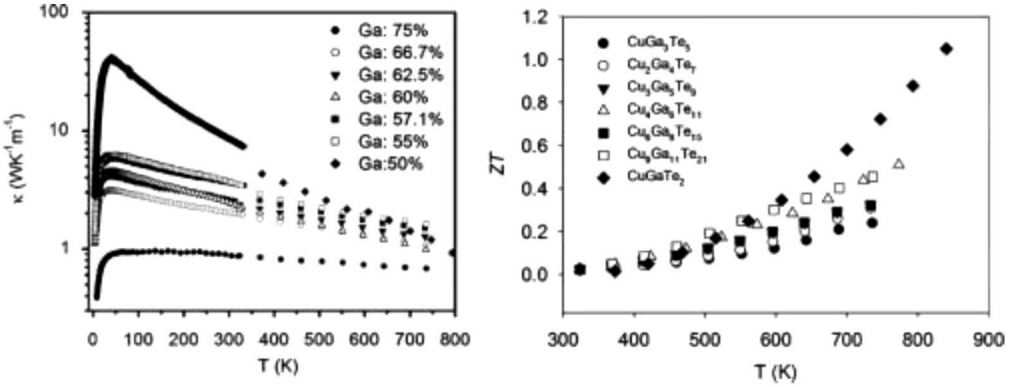

Highlights

► All the samples show p-type semiconducting behavior in the temperature dependence of the Seebeck and Hall coefficients. ► The increased carrier concentration and the introduction of vacancies diminish the carrier mobility and power factor. ► The low temperature k decreases significantly as the Ga_2Te_3 content increases due to increasing point defects. ► The highest ***ZT*** ~ 1.0 at 840 K among the samples in this study was found in CuGaTe2, which contains no vacancies.

Temperature-dependent XRD, IR, magnetic, SEM and TEM studies of Jahn–Teller distorted $NiCr_2O_4$ powders

Original Research Article

Pages 270-279

M. Ptak, M. Maczka, A. Gągor, A. Pikul, L. Macalik, J. Hanuza

Graphical abstract

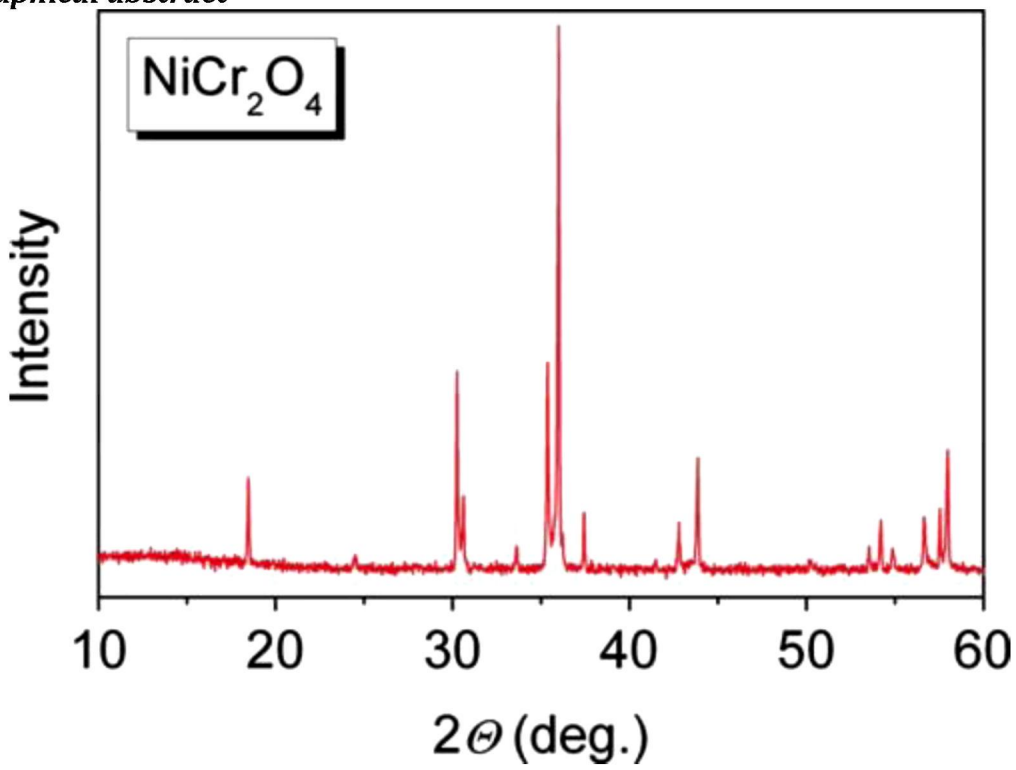

Correlation between processing conditions, microstructure and charge transport in half-Heusler alloys

Original Research Article

Pages 280-287

Julien P.A. Makongo, Xiaoyuan Zhou, Dinesh K. Misra, Ctirad Uher, Pierre F.P. Poudeu

Graphical abstract

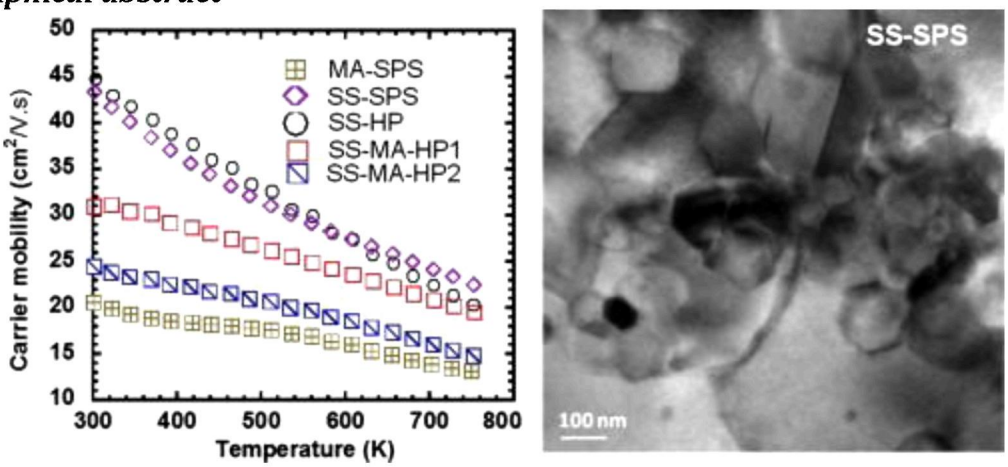

Highlights

► Phase composition of HH alloy strongly depends on the synthesis technique. ► Mechanical alloying of elements yields bulk HH alloy with metallic impurity phases. ► Thermopower, carrier density, and effective mass of HHs are insensitive to processing conditions. ► Mechanical alloying decreases the carrier mobility and lattice thermal conductivity of bulk HH.

Crystal structure, growth and characterization of $LiPbB_9O_{15}$: A new congruent melting nonlinear optical crystal

Original Research Article

Pages 288-292

M.J. Xia, R.K. Li

Graphical abstract

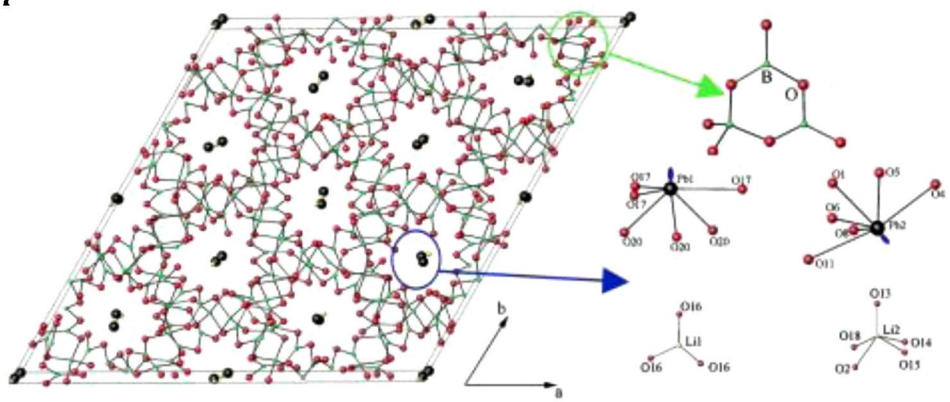

Crystal and electronic structures of the new quaternary RCr_3Si_2C (R=Y, Gd–Tm, Lu, U) compounds

Original Research Article

Pages 293-301

Pierric Lemoine, Janusz Tobola, Anne Vernière, Bernard Malama

Graphical abstract

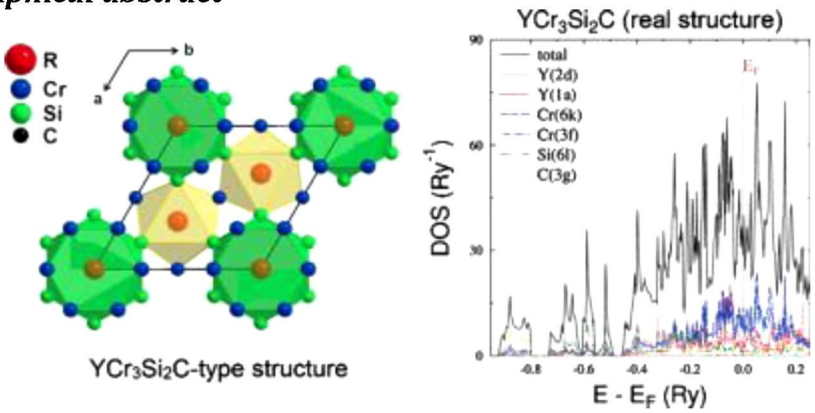

Highlights

► Crystal structure determination of the new intermetallic YCr_3Si_2C compound. ► New type-structure closely related to the YCo_3Ga_2-type. ► Theoretical study of the structural stability by electronic structure calculations. ► Crystal structure characterization of the entire ***R***Cr_3Si_2C series

Eu-doped α-Fe_2O_3 nanoparticles with modified magnetic properties

Original Research Article

Pages 302-311

Francesca Stefania Freyria, Gabriele Barrera, Paola Tiberto, Elena Belluso, Davide Levy, Guido Saracco, Paolo Allia, Edoardo Garrone, Barbara Bonelli

Graphical abstract

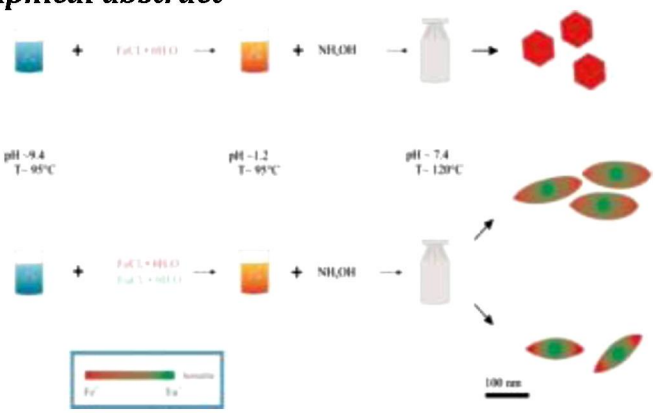

Synthesis, crystal and electronic structures and magnetic properties of $Li_2SnMo_3O_8$: A novel reduced molybdenum oxide containing Mo_3O_{13} cluster units

Original Research Article

Pages 312-316

Philippe Gall, Rabih Al Rahal Al Orabi, Thierry Guizouarn, Jérôme Cuny, Bruno Fontaine, Régis Gautier, Patrick Gougeon

Graphical abstract

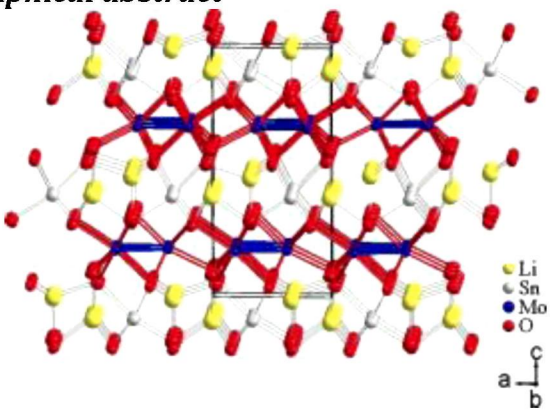

Synthesis and magnetization studies of nanopowder $Fe_{70}Ni_{20}Cr_{10}$ alloys prepared by high energy milling

Original Research Article

Pages 317-323

R. Chater, M. Bououdina, D. Chaanbi, H. Abbas

Graphical abstract

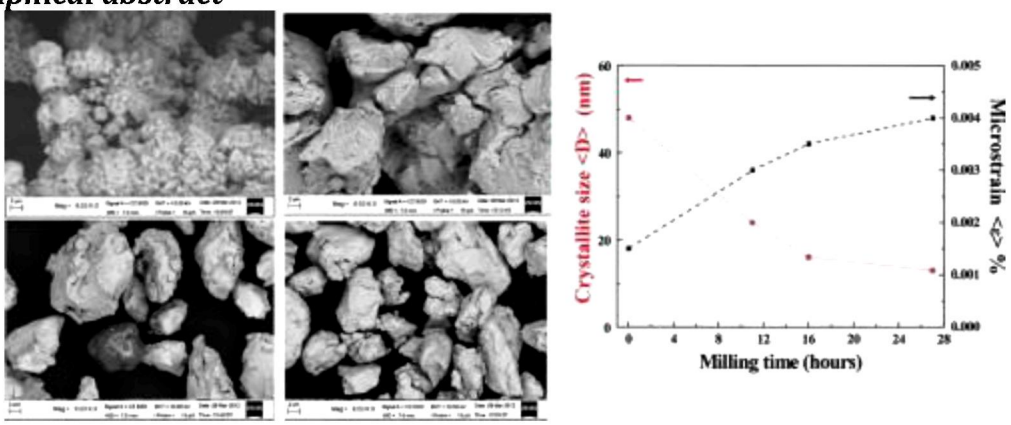

Structural consideration on the emission properties of Eu^{2+}-doped $Ba(Sr, Ca)_2MgSi_2O_8$

Original Research Article

Pages 324-329

Yoshinori Yonesak

Graphical abstract

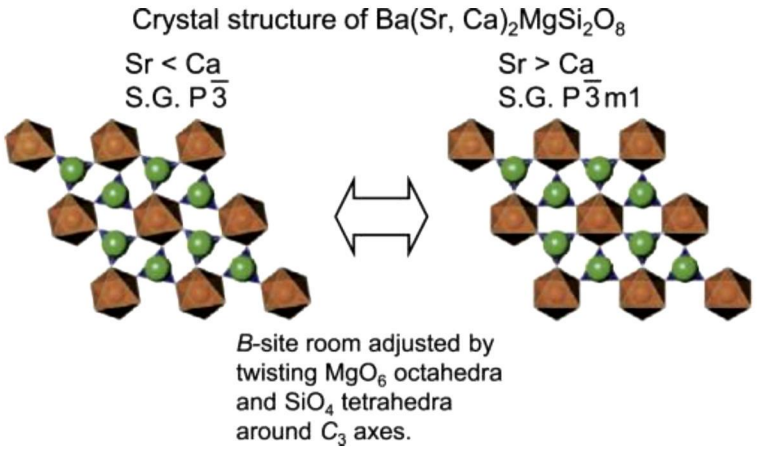

Highlights

·► Glaserite-type $Ba(Sr, Ca)_2MgSi_2O_8$ has been prepared by a solid state reaction.·► $Ba(Sr, Ca)_2MgSi_2O_8$ changes the crystal structure, depending on Sr/(Sr+Ca) ratio.·► Eu^{2+}-doped $Ba(Sr, Ca)_2MgSi_2O_8$ exhibits blue emission under ultraviolet irradiation.·► Emission from $Ba(Sr, Ca)_2MgSi_2O_8$ is characterized by two Eu^{2+} emission components.·► The two emissions show wavelength shift in a similar manner against Sr/(Sr+Ca).

Scalable synthesis of Fe_3O_4 nanoparticles anchored on graphene as a high-performance anode for lithium ion batteries

Original Research Article

Pages 330-337

Yu Cheng Dong, Ru Guang Ma, Ming Jun Hu, Hua Cheng, Chun Kwan Tsang, Qing Dan Yang, Yang Yang Li, Juan Antonio Zapien

Graphical abstract

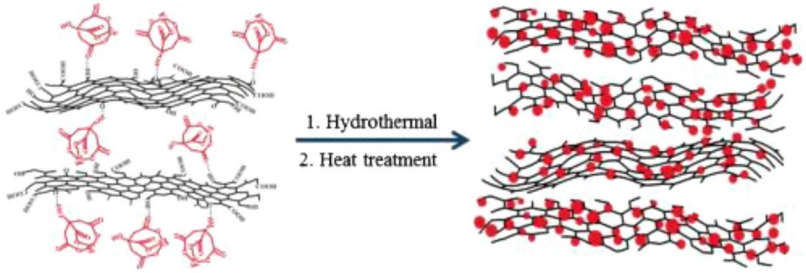

Highlights

► Fe_3O_4/graphene composites are synthesized directly from graphene and $C_6H_5FeO_7$. ► The citrate function as reductant and anchor agent in this reaction process. ► The resulting Fe_3O_4 particles (~4–16 nm) are densely anchored on graphene sheets. ► The prepared Fe_3O_4/graphene composites exhibit excellent electrochemical performance.